Journal of Hydrology 681 (2026) 136632

Contents lists available at ScienceDirect

Journal of Hydrology

journal homepage: www.elsevier.com/locate/jhydrol

Complex behavior of an urban green infrastructure imaged using time-lapse electrical resistivity tomography and time-series clustering

Alexis Luzy[a,*], Adrien Dimech[a], François Duhaime[a], Janie Masse-Dufresne[a], Jean-Sébastien Dubé[a], Rose-Anne Farley[a], Rémi Clément[b], Maxime Paradis[c]

[a] École de technologie supérieure, Montréal, Québec, Canada
[b] INRAE, REVERSAAL, Villeurbanne, 69100, France
[c] Service de l'ingénierie, City of Laval, Québec, Canada

HIGHLIGHTS

- High-density cross-borehole arrays effectively monitor complex urban subsurface.
- Time-series clustering efficiently complements hydrogeochemical interpretation.
- Open-source hardware enables high-quality, low-cost long-term monitoring.
- Green infrastructure influences salt infiltration dynamics.

ARTICLE INFO

This manuscript was handled by Dongmei Han, Editor-in-Chief, with the assistance of Deqiang Mao, Associate Editor

Keywords:
Hydrogeophysics
TL-ERT
Cross-borehole ERT
Green infrastructure
Road de-icing salt

ABSTRACT

Urban green infrastructure (GI) is increasingly being implemented to manage stormwater, promote infiltration, and limit loads on drainage networks. However, their design still relies largely on large-scale hydrological performance, with limited attention to site-specific hydrogeological processes. Key mechanisms governing infiltration, solute transport, and seasonal dynamics remain poorly understood, especially in cold-climate cities using de-icing salts, which may threaten buried infrastructure, contribute to groundwater salinization, and degrade receiving ecosystems. Field observations are needed to improve understanding of these processes. This study presents one year of monitoring of water and chloride dynamics around an instrumented GI using high-resolution cross-borehole time-lapse electrical resistivity tomography (TL-ERT) at a roadside site in Laval, Quebec, Canada. Automated geoelectrical monitoring was conducted between October 2024 and November 2025 with four surveys per day, using commercial and open-source hardware. The geophysical approach was complemented by hydrogeological monitoring (water levels and sensors). A time-series clustering method was applied to the inverted dataset to identify distinct temporal behaviors of subsurface units. Results indicate infiltration linked to winter rainfall and spring snowmelt. Seasonal conductivity variations in winter and spring are interpreted as being largely influenced by pore-water conductivity associated with de-icing salt mobilization, while late summer and autumn changes are more consistent with VWC-driven responses. Overall, combining cross-borehole TL-ERT, time-series clustering, and hydrogeological instrumentation provides detailed insight into seasonal water and solute movement in small-scale, heterogeneous urban environments, where point monitoring is often limited. This approach is well suited for studying urban GI, while remaining dependent on auxiliary measurements for process attribution.

1. Introduction

Urban stormwater management is increasingly challenged by the cumulative effects of climate change, rapid urbanization, aging drainage infrastructure, and high impervious surface cover (Sterling et al., 2013; Bhaskar et al., 2016; Gogien et al., 2023). These factors generate excess surface runoff that strains urban water systems, pushing municipalities to prioritize broader surface runoff reduction strategies at the source (MELCCFP, 2023). Within this context, combined sewer

* Corresponding author.
Email address: alexis.luzy.1@ens.etsmtl.ca (A. Luzy).

https://doi.org/10.1016/j.jhydrol.2026.136632
Received 16 April 2026; Received in revised form 30 September 2026; Accepted 14 October 2026
Available online 15 October 2026
0022-1694/© 2026 The Author(s). Published by Elsevier B.V. This is an open access article under the CC BY license (http://creativecommons.org/licenses/by/4.0/).

overflows (CSOs) represent a growing challenge in many large cities (Perry et al., 2024), as combined systems can be forced to discharge wastewater and stormwater when hydraulic capacity is exceeded during intense rainfall or winter snowmelt (Mailhot et al., 2015; Teufel and Sushama, 2021). This issue is expected to become even more critical as North American climate models predict a 10% to 20% increase in the frequency and intensity of extreme precipitation (Nodine et al., 2024).

The consequences of inadequate stormwater management extend beyond hydraulic performance (Botturi et al., 2021). Conventional drainage of road runoff routinely introduces suspended solids, metals, hydrocarbons, and de-icing salts directly into soils and receiving waters (Corsi et al., 2010). This heavy chemical loading is particularly concerning, as chloride and sodium accumulation has increasingly been linked to severe lake salinization and long-term groundwater degradation (Mackie et al., 2022; Radosavljevic et al., 2024). Furthermore, when excess runoff triggers CSOs, these events represent a primary source of surface aquatic ecosystem contamination (Gooré Bi et al., 2015), facilitating the direct transfer of untreated wastewater and various pollutants into the environment (Olds et al., 2018). From a public health perspective, microbial contamination during overflows can exceed safety thresholds by several orders of magnitude (Madoux-Humery et al., 2013). Beyond ecological risks, these challenges impose a staggering financial burden due to aging and undersized infrastructure (Perry et al., 2024). For instance, the remnants of Hurricane Debby in August 2024 caused record flooding in Quebec, becoming the province's most expensive climate event, with nearly $2.5 billion in insured damages (BAC, 2024).

To mitigate pressure on urban sewer systems, many cities are increasingly adopting nature-based solutions (NBS), of which GI is a key subset (Fletcher et al., 2015). These engineered systems can include bioswales, bioretention cells, rain gardens, and other infiltration or filtration designs. Some systems promote infiltration into the native subsurface, whereas others rely on underdrains that return treated water to the stormwater network. This distinction determines the extent of groundwater recharge and subsurface solute transport. Catchment-scale modelling suggests that optimized GI implementation could substantially reduce overflow volumes (Torres et al., 2021; Jean et al., 2021, 2022). In addition to helping manage peak flows, GIs also contribute to the management of contaminants (Deeb et al., 2020; Spraakman and Drake, 2021). For example, bioretention systems temporarily attenuate winter road salt loads to the sewer system but largely transfer Na^+ and Cl^- to groundwater (Burgis et al., 2020; Denich et al., 2013). Other studies have documented high retention capacities for heavy metals such as chromium, lead, and zinc (Paus et al., 2014; Beral et al., 2023). By temporarily retaining stormwater, GIs act as a buffer that enhances the robustness of urban water management strategies (Chen et al., 2019).

Despite their widespread adoption, the in situ performance of GI remains difficult to evaluate due to as-built variability (Le Gigan et al., 2025) and heterogeneous subsurface conditions (Kaushal and Belt, 2012; Kwak et al., 2024). Hydrogeologically, GI systems exhibit substantial variability in in situ saturated hydraulic conductivity (Spraakman and Drake, 2021) and can locally alter hydraulic heads (Tu and Traver, 2019). The monitoring of these dynamics remains challenging: conventional instrumentation, such as point-scale sensors and piezometers, often lacks the spatial representativeness required to accurately characterize subsurface processes in complex and spatially variable systems such as urban GIs (Vereecken et al., 2008; Mason et al., 2023; O'Brien et al., 2024). From a geochemical standpoint, GI may also act as a pathway for groundwater contaminants (Burgis et al., 2020; Denich et al., 2013), potentially leading to the corrosion of subsurface pipe networks (Pieper et al., 2018; Song et al., 2017) and groundwater pollution (Mackie et al., 2022; Mayer et al., 1999; Corsi et al., 2010). Furthermore, assessing these geochemical dynamics remains complex, as lysimeters and groundwater sampling campaigns are time-consuming, spatially limited, and influenced by subsurface heterogeneity and installation methods (Fares et al., 2009; Singh et al., 2018). Overall, when combined with the inherent complexity of urban subsurface processes (Shuster et al., 2021; Bonneau et al., 2018), these limitations suggest that conventional instrumentation alone is insufficient to comprehensively characterize water infiltration, solute movement, seasonal storage, and drainage processes within and adjacent to GI systems.

Time lapse electrical resistivity tomography (TL-ERT) can overcome the spatial and temporal limitations of traditional methods by providing continuous, indirect imaging of the cumulative effects of subsurface water and solute dynamics through changes in the electrical conductivity of the medium, hereafter referred to as bulk EC (Hermans et al., 2023; Dimech et al., 2022, 2024). Recent applications in urban environments demonstrate the relevance of surface ERT in tracking subsurface salt plumes, with an emphasis on TL-ERT (Hodgins et al., 2023, 2024; Pope et al., 2025). Cross-borehole configurations allow for high spatial resolution at depth (Kuras et al., 2009; Grünenbaum et al., 2023) and have already been used for the precise tracking of saline plumes (Slater et al., 2000; Perri et al., 2012). Recently, the OhmPi Project (Clement et al., 2020; Blanchy et al., 2024) has provided an efficient solution to promote TL-ERT integration with hydrogeological monitoring programs, offering an affordable alternative for geoelectrical monitoring and it has been identified as a key aspect for future TL-ERT applications and developments (Slater and Binley, 2021; Dimech et al., 2022).

Aiming to bridge the gap between geophysical observations and hydrogeological interpretation, time-series clustering (TSC) offers a robust approach for condensing multidimensional TL-ERT data into groups of similar spatial and temporal variations (Aghabozorgi et al., 2015; Jain et al., 1999). By delineating zones with similar temporal patterns, TSC can facilitate the identification of hydrofacies and geological structures in a more objective way (Delforge et al., 2021; Oladeji et al., 2024) and it has demonstrated effectiveness in complex karst environments (Xu et al., 2017).

This study investigates how an infiltration-based roadside GI and its surrounding urban subsurface respond to individual rainfall events, winter de-icing salt inputs, and spring snowmelt. Specifically, the objectives are to image the spatial and temporal distribution of bulk EC using high-resolution cross-borehole TL-ERT, identify subsurface zones with distinct seasonal dynamics using time-series clustering, and interpret the observed bulk EC variations in terms of water dynamics and chloride-related pore-water conductivity. To our knowledge, this represents one of the first urban GI sites monitored with this level of cross-borehole spatial resolution using open-source instrumentation. This study provides a first step toward a more process-based understanding of subsurface hydrological and solute transport dynamics in infiltration-based GI systems and their interaction with groundwater systems.

2. Methodology

2.1. Study site

Fig. 1 presents the instrumented GI located in Laval, Quebec, Canada, constructed in summer of 2023. The GI includes an underdrain which is expected to limit hydraulic connectivity between infiltrated water and the underlying native subsurface. Monitoring instrumentation includes a cross-borehole electrical resistivity tomography profile and two additional hydrogeological monitoring profiles. As presented in Fig. 1 a), the GI features a rectangular geometry measuring 2 m in width by 50 m in length, with an approximate depth of 1 m. The installation is bounded by a concrete sidewalk on one side and asphalt pavement on the other. It should be noted that the adjacent roadway exhibits a major longitudinal crack exceeding 10 cm in width at several locations, approximately 3 m from the center of the GI. Stormwater enters the system in three locations (Fig. 1 a) through lowered curb openings and overflow outlets connected to sediment traps (Fig. 1c), both discharging runoff into the bioretention area.

Fig. 1 f) displays the particle size distribution (PSD) curves of the samples analyzed following the method of BNQ 2501-025/2013, with Fig. 1 b) showing the sampling locations marked with stars. The PSD curves highlight three distinct material types. The brown curves (9

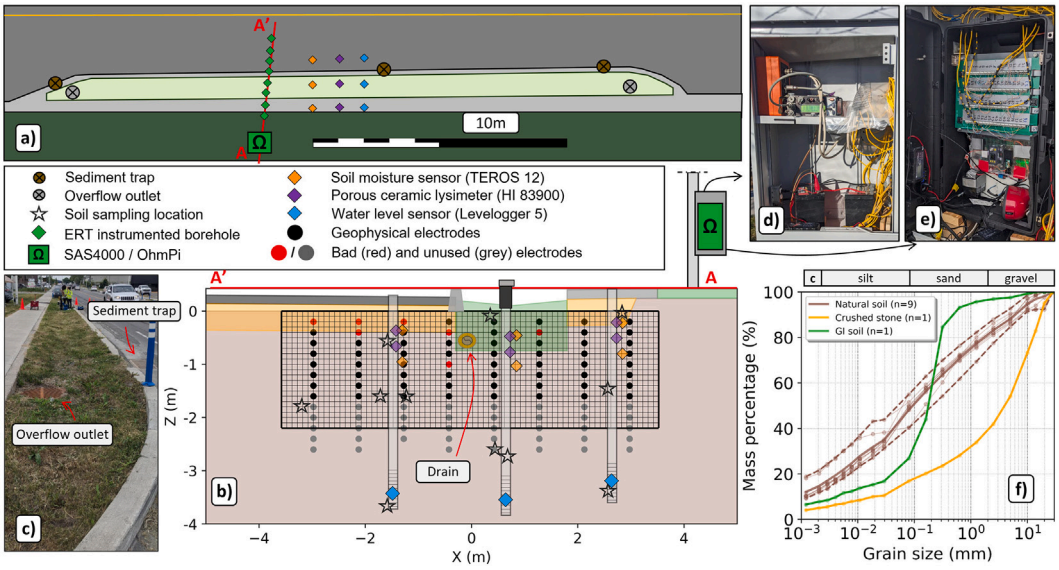


Fig. 1. Studied site with a) plan view the GI and of the three instrumented profiles, b) cross-section view of the ERT profile showing borehole electrodes, piezometers and sensor positions. c) lengthwise view of the GI with the sediment trap and overflow outlet. The ERT instrumentation setup is shown in d) for the SAS4000 and e) for the OhmPi (measurement board version 2024). f) particle size distributions of the samples retrieved at the locations marked by stars, "c" stands for the clay particle size range.

samples) correspond to a well-graded natural till deposit. In contrast, the green curve (1 sample), corresponding to the GI material, shows uniform grading, with roughly 70% (w/w) retained between the 80 μm and 1.25 mm standard sieves, and around 25% (w/w) passing 80 μm. The yellow curve (1 sample), associated with the crushed-stone layer beneath the road and sidewalk, corresponds to a coarse material, with about 35% (w/w) passing 1.25 mm. Fig. 1 f) shows that the three soils display distinct particle-size distributions, which are expected to translate into contrasting hydrogeological behaviors due to differences in grading, porosity, and pore connectivity.

These different PSDs are reflected in measured hydraulic properties across the system. *In situ* measurements using a Guelph permeameter (model 2800K1, Soil Moisture) yielded a saturated hydraulic conductivity of approximately 3×10^{-6} m/s for the GI soil. This value is lower than the 8×10^{-6} to 55×10^{-6} m/s range (30 to 200 mm/hr) commonly reported in recent local design guidance for full-infiltration street GI (Dugué, 2022). In contrast, variable-head tests conducted in the three piezometers using the method from Chapuis (1999) indicated a much lower mean hydraulic conductivity of 4×10^{-8} m/s for the underlying till. These contrasting values are important for interpreting the TL-ERT response, as they suggest greater infiltration capacity within the engineered GI material, but limited drainage into the native till.

2.2. Hydrogeological and geophysical instrumentation

The GI was constructed prior to the start of the project. Geophysical electrodes were installed at the beginning of December 2023, along with sensors and lysimeters in the vadose zone and piezometers in the saturated zone. In Fig. 1(a), the first profile (green) corresponds to the cross borehole ERT installation. The second profile enables point measurements of soil volumetric water content (VWC), bulk EC, and temperature using TEROS 12 sensors (METER Inc.), installed at depths of 60 cm and 120 cm from the surface (in orange in Fig. 1 a and b). The TEROS 12 dataset contained frequent gaps, and water was periodically found inside the below-ground access tubes. Together with inconsistent VWC and bulk EC responses, these raised concerns about the reliability of these measurements. Consequently, only the temperature data were used in this study. The third profile corresponds to the porous ceramic lysimeters (Hanna Instruments, HI83900-60 and 90) which were installed at 60 cm and 90 cm to allow for monthly unsaturated zone water sampling (in purple in Fig. 1 a and b) that began in summer 2025 following an initial testing period. As a result, a sufficiently long and comparable time series was not yet available for the monitoring period investigated in this study. Finally, groundwater levels, temperature, and EC were monitored using conventional piezometers equipped with water level, temperature, and conductivity (LTC) sensors (Levelogger 5, Solinst, see blue diamonds in Fig. 1 a and b).

Fig. 1 b) displays the geometry of the geophysical profile. The ERT installation consists of eight boreholes positioned at 85 cm intervals, each instrumented with 13 geophysical electrodes, except for one which had only twelve due to drilling refusal. Each electrode borehole was fabricated using 2.7 m long PVC tubing with an 38 mm outer diameter, following the method used in Sylvain et al. (2019); Dimech et al. (2023). Stainless steel electrodes (2 cm long by 4 cm in diameter) are installed at 20 cm vertical intervals and connected to the ERT acquisition hardware from inside the tubing using stainless steel rivets (Dimech et al., 2023).

Ensuring good electrical contact between the electrodes and the surrounding soil is essential to maintain low contact resistance and obtain reliable measurements (Ingeman-Nielsen et al., 2016). To achieve this, a cement–bentonite grout backfill was used, following recommendations by Doetsch et al. (2010), Thomle et al. (2023) and Mikkelsen (2002). The electrode borehole pipe was then pushed into the grout-filled borehole casing, following the procedure described in Luzy et al. (2024). The spatial layout of the array covers an area of approximately 6 m wide and 2.4 m high, chosen to fully encompass the expected infiltration and flow zones. The proper functioning of the electrode array was tested in March 2024 using the methodology described in Luzy et al. (2024).

2.3. ERT data acquisition

The TL-ERT dataset was acquired using two independent systems shown in Fig. 1, d) and e). A Terrameter SAS4000 (ABEM) recorded 508 surveys from October 4, 2024, until the installation of the OhmPi system (Clement et al., 2020), with a temporary interruption in data acquisition between December 4, 2024, and January 20, 2025. The OhmPi device began operating on April 16, 2025, acquiring one survey every 6 hours. As of April 2026, it had completed 1350 surveys.

The measurement protocol is based on bipole–bipole configurations, following the approaches of Kuras et al. (2009) and Clément et al. (2014). As illustrated in the bottom left part of Fig. 2, current is injected

using electrodes positioned at similar depths either in the adjacent boreholes (bipole-bipole, referred to as BB0) or in the next boreholes (skipped bipole-bipole or SBB0). Potentials are measured using the first or second (BB1 or SBB1) electrode directly below the current dipole. A complete survey consists of 286 measurements, including configurations using the third or fourth electrode below the injection bipole, which are not processed due to their much higher sensitivity to noise.

The ERT hardware is installed in a grounded street-lighting electrical box connected to a continuous 120 V power supply. This setup enables safe year-round operation of the monitoring system and allows a heater to be used during winter to maintain reliable operation under freezing conditions. Due to hardware limitations, only 64 of the 103 installed electrodes are used (unused electrodes are shown in grey in Fig. 1b), although the OhmPi could have been connected to more electrodes (Blanchy et al., 2024).

2.4. Data quality

Robust data quality assessment is essential for obtaining reliable inversion results (LaBrecque et al., 1996; Slater et al., 2000). As shown in Tso et al. (2017), reciprocal measurements are considered the most reliable way to assess measurement quality, while other methods, like stacking error, tend to underestimate it. Starting in mid-April 2025, a daily reciprocal survey is conducted with the OhmPi hardware, with reciprocal error e (%) computed as follows from Tso et al. (2017):

$$e = \frac{|R_N - R_R|}{|R_N + R_R|} \times 100 \tag{1}$$

The terms R_N and R_R are the normal and reciprocal resistance values, respectively. In ideal conditions, these values should be equal (Parasnis, 1988), with any deviation attributable to measurement noise and systematic errors (LaBrecque et al., 1996). Electrodes that repeatedly produce outliers or measurements with $e > 10\%$ are removed from the protocol, a threshold employed in previous studies (Uhlemann et al., 2016; Dimech et al., 2023). This process identifies dysfunctional electrodes, one with the SAS4000 and seven with the OhmPi, mostly located in the crushed stone layer beneath the road and displaying high contact resistances (highlighted in red in Fig. 1 b). All measurements involving these electrodes are discarded, resulting in final datasets comprising 162 quadrupoles for the SAS4000 surveys conducted in autumn 2024 and 118 quadrupoles for the OhmPi surveys (see Fig. 3).

2.5. Inversion

All ERT datasets are inverted individually using the inversion framework from the open-source Python library pyGIMLi (Rücker et al., 2017). The mesh is a 2D grid with a cell size of 10 × 10 cm, resulting in a mesh of 1562 elements. Each time step is inverted independently to preserve sharp conductivity changes after rainfall events, avoiding oversmoothing effects associated with temporal regularization (Loke et al., 2014). The inversion seeks to minimize the standard smoothness-constrained cost function:

$$\Phi(\mathbf{m}) = \left\|\mathbf{W_d} \cdot (\mathbf{F}(\mathbf{m}) - \mathbf{d})\right\|^2 + \lambda \left\|\mathbf{W_m} \cdot (\mathbf{m} - \mathbf{m}_0)\right\|^2 \tag{2}$$

The first term, $\left\|\mathbf{W_d} \cdot (\mathbf{F}(\mathbf{m}) - \mathbf{d})\right\|^2$, quantifies the data misfit, with $\mathbf{F}(\mathbf{m})$ being the forward response to a given model $\mathbf{m}$, and $\mathbf{d}$ the observed data. $\mathbf{W_d}$ is a diagonal matrix of inverse reciprocal errors, serving as a weighting matrix that accounts for data uncertainties. The second term, $\lambda \left\|\mathbf{W_m} \cdot (\mathbf{m} - \mathbf{m}_0)\right\|^2$, imposes spatial regularization to stabilize the inversion, where $\mathbf{m}_0$ is the reference model, and λ controls the balance between data fidelity and model smoothness, which is set to 20. $\mathbf{W_m}$ is the model roughness matrix, incorporating the anisotropic regularization of Jordi et al. (2018), implemented in pyGIMLi with the zWeight parameter set to 0.75 to lightly favor vertical gradients during inversion. All inversions converge rapidly, reaching normalized misfits χ^2 close to 1 (except in winter) within three iterations (see Supplementary Figure S1).

2.6. Temperature correction

Seasonal variations in subsurface temperature significantly influence geoelectrical imaging (Hayley et al., 2007), especially in Canada, where yearly temperatures span from −15 °C to + 30 °C. A correction to a reference temperature is then necessary to ensure accurate interpretation and comparability across several months of data (Dimech et al., 2023; Uhlemann et al., 2016). In this study, temperature correction is applied to inverted ERT results using a thermal model taken from Brunet et al. (2010) to predict the temperature in the soil at any depth z and time t.

$$T(z,\ t) = T_{\text{mean}} + \frac{\Delta T}{2} \exp\left(-\frac{z}{d}\right) \sin\left(\frac{2\pi}{365} t + \boldsymbol{\phi} - \frac{z}{d}\right) \tag{3}$$

where T_{mean} is the annual mean surface temperature, ΔT is the amplitude of seasonal variation, d is the thermal damping depth, and $\boldsymbol{\phi}$ is the phase offset. Seasonal temperature measurements are obtained using TEROS 12 sensors depicted in Fig. 1, each located in a different surface setup: a paved road, a GI, and a concrete sidewalk. Given the highly variable thermal behavior of these three vertical profiles, the model from Eq. (3) is fitted independently for each borehole using data from the sensors. All four parameters from Eq. (3) are estimated for each borehole to replicate the observed data. R^2 values above 0.98, $RMSE$ values below 0.9 °C, and absolute residuals under 2 °C are obtained (see Supplementary Figures S4, S5 and S6).

The 3 different vertical models obtained are then extrapolated to yield a complete $x - z$ temperature distribution. As in Uhlemann et al. (2016), temperature-corrected bulk EC values (σ_{corr}) are computed using a temperature-conductivity relation of the form:

$$\sigma_{t,\ \text{corr}} = \frac{\sigma_{\text{t, raw}}}{1 + c\left(T_{target} - T_{\text{t, modeled}}\right)} \tag{4}$$

where $\sigma_{\text{t, raw}}$ is the non-corrected bulk EC distribution at time t, $T_{\text{target}} = 25$ °C corresponds to the reference temperature, and $T_{\text{t, modeled}}$ corresponds to the $x - z$ temperature distribution at time t, computed with Eq. (3). c is the temperature sensitivity coefficient. In this study, a value of 0.02 °C^{-1} is used, as reported in Chambers et al. (2014). This relationship has been shown to effectively correct bulk EC across temperatures from 3 to 47 °C (Ma et al., 2011).

2.7. Time-lapse clustering

To delineate zones of similar behavior or properties, the Hierarchical Agglomerative Clustering (HAC) method is used, as in Xu et al. (2017). Scikit-learn's HAC implementation (Pedregosa et al., 2011), is preferred since it offers the option of including a connectivity matrix (Abraham et al., 2014) to restrict cluster fusions to spatially adjacent samples, preserving spatial coherence. As proposed in Delforge et al. (2021), the time series are log transformed and z-standardized using the following formula:

$$\mathbf{X_{z,i}} = \frac{\mathbf{X_i} - \mu(\mathbf{X_i})}{\sigma(\mathbf{X_i})} \tag{5}$$

where $\mathbf{X_i}$ is the log-transformed time series of EC values extracted at position (x, z) from a set of inverted models. $\mu(\mathbf{X_i})$ and $\sigma(\mathbf{X_i})$ are, respectively, the mean and standard deviation of $\mathbf{X_i}$. This preprocessing is done to ensure scale invariance prior to applying the HAC algorithm.

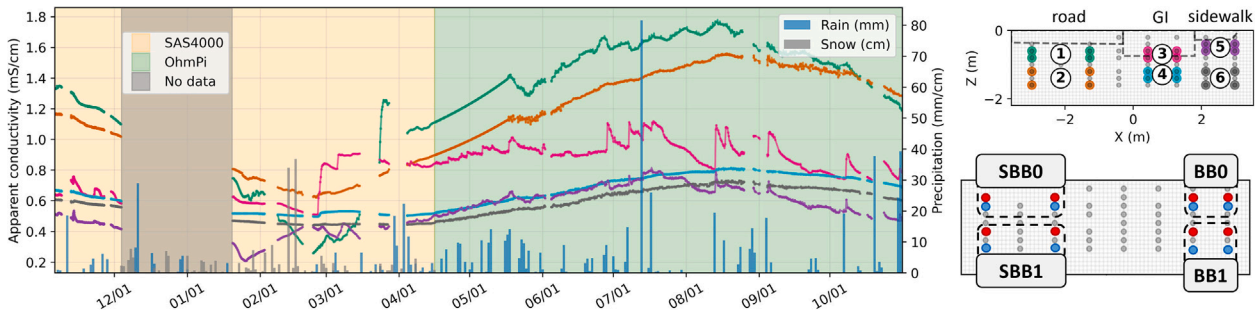


Fig. 2. Raw measured apparent conductivities (left axis) and daily precipitation (right axis, data from environment and climate change Canada) from November 5, 2024, to November 1, 2025. These time series are sampled from six configurations, as displayed on the top right panel. The background indicates which ERT hardware device is used. Bottom right panel shows the 4 types of configurations kept for the inversion process.

3. Results

3.1. Raw time-lapse apparent conductivity

Fig. 2 displays raw apparent conductivity time series acquired at six positions from November 5, 2024, to November 1, 2025. The dataset includes a gap from early December 2024 to late January 2025, during which no data are acquired, along with several shorter interruptions later in 2025 due to hardware problems, for a total of 1209 surveys. Gaps shorter than three and a half days are interpolated (see Supplementary Figure S2). All uncorrected time series exhibit a sinusoidal pattern over the course of a year, reflecting seasonal temperature variations with amplitudes that depend on location. Interestingly, while the configurations below the road and sidewalk show a clear decrease in apparent conductivity during winter, when near-surface temperatures approach 0 °C, raw measurements at the bottom of the GI do not display a similar pattern. Furthermore, temperature-induced apparent conductivity variations seem to persist even at depths exceeding 1.5 m, highlighting the necessity for temperature correction of the inverted models to allow for proper comparison across extended periods.

Surface measurements (Fig. 2, time series 1, 3, and 5) reveal specific responses to precipitation events, characterized by sharp apparent conductivity variations following rainfall. This behavior is most pronounced for the configuration beneath the GI, slightly weaker under the sidewalk, and nearly absent under the road. Furthermore, these sharp variations predominantly occurred from mid-summer onward, suggesting a shift in the mechanisms controlling apparent conductivity. Despite the hardware change between the two acquisitions, the time series remains highly consistent, indicating both the robustness of the dataset and the apparent conductivity dynamics observed along the profile.

3.2. Temperature-corrected static bulk EC distribution

Fig. 3 presents two inverted and temperature-corrected bulk EC images acquired approximately one year apart. Both models show a similar distribution of bulk EC. In the first 50 cm, a relatively low EC layer is observed, particularly beneath the sidewalk and the asphalt pavement, with values between 0.1 and 0.4 mS/cm. The soil in the depth range of –0.5 m to –1.25 m reveals a heterogeneous pattern, below the curb, a moderately conductive layer is visible (0.4 to 0.7 mS/cm), the leftmost portion of the profile exhibits a much more conductive zone, with values between 1.0 and 1.6 mS/cm beneath the road, slightly decreasing at greater depths.

The primary difference between the two models lies in the upper 50 cm layer beneath the road, which is less resolved and shows higher conductivities in the 2025 image, mainly because of the five electrodes that were removed due to high contact resistance. Therefore, the crushed stone layer under the road will be masked and excluded from further analysis. Despite the reduced local sensitivity (see Supplementary Figure S3), the overall sensitivity of the protocol remains very high, enabling reliable characterization of subsurface bulk EC dynamics (Fig. 3). The key feature in both images is the pronounced conductivity gradient toward the left, consistent with the observed water table gradient and with groundwater EC and chloride measurements sampled in the piezometers (see Supplementary Figures S9 and S10).

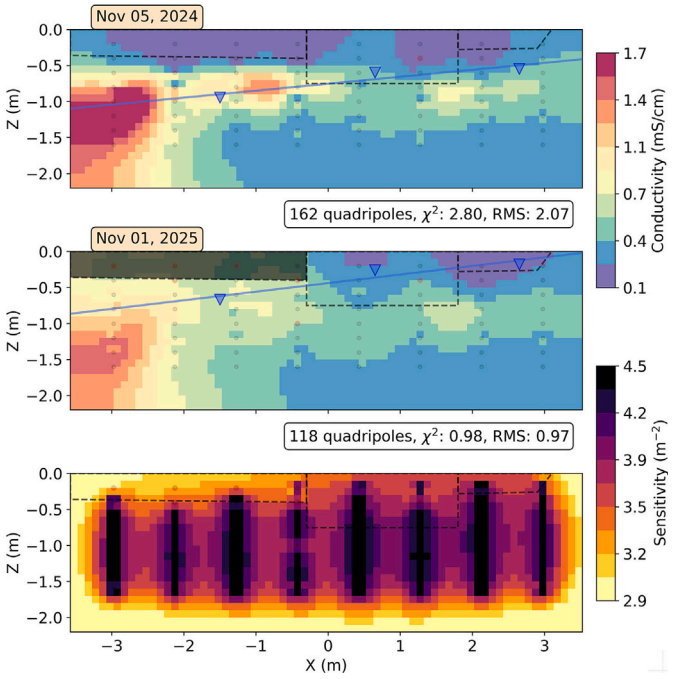


Fig. 3. Inverted and temperature-corrected bulk EC images obtained on November 5, 2024 (top) and November 1, 2025 (middle). The blue line represents the extrapolated water table from the three measured points. Bottom row shows the measurement protocol sensitivity after removing the dysfunctional electrodes. (For interpretation of the references to colour in this figure legend, the reader is referred to the web version of this article.)

3.3. Time-lapse seasonal imaging

Fig. 4 illustrates seasonal variations in bulk EC along the monitored profile. The figure shows corrected bulk EC images sampled on six dates throughout the year, with their relative variations from t_0 in %. The top time-series panel is shown to support the patterns suggested by the sparse spatial images. Despite substantial temporal changes, the spatial distribution of bulk EC remains consistent throughout the year, with higher values on the left and around the water table and lower values on the right, in agreement with the static images shown in Fig. 3.

The bottom row displays conductivity change $\Delta\sigma_i$ in % relative to the baseline distribution at t_0 on November 5th, 2024, computed as:

$$\Delta\sigma_i = (\sigma_{\mathrm{corr},i}/\sigma_{\mathrm{corr},0} - 1) \times 100 \quad (6)$$

At the start of winter (t_1/t_0), a significant EC increase occurs in the GI (from 60% to over 100%), while the zone beneath the sidewalk and road initially shows a considerable decrease (60 to 80%), which is interpreted as partially frozen soil. By late February (t_2/t_0), bulk EC starts to diminish again in the GI and sidewalk areas, though a distinct increase begins to develop beneath the road surface. Starting from April 15 (t_3/t_0), following the pronounced reduction in GI bulk EC, the overall trend moderates as variations in near surface decrease. The subsequent time steps (t_4 and t_5) exhibit a slow, continuous decline in bulk EC, eventually reaching the t_5/t_0 ratio. This late image exhibits only shallow variations, concentrated below the sidewalk, with a much higher water table than in November 2024. These results indicate a broad seasonal cycle in bulk EC over the year, with several responses associated with temperature fluctuations in autumn, snow accumulation and winter rainfall and snowmelt in late winter (e.g., mid-February and March, see Supplementary Figure S7).

3.4. Rainfall events imaging

Fig. 5 illustrates changes in conductivity following five rainfall events during the monitoring period. These intervals were chosen to capture the temporal evolution of rainfall-induced conductivity changes across the profile. The bulk EC variations following these precipitation events exhibit two main patterns.

The first kind of pattern, observed during the autumn events (rainfall events 1, 4, and 5 in autumn 2024 and 2025), is characterized by conductivity variations occurring above the water table. Following a rain event, there is a rapid bulk EC increase of 6 to 20% in the GI and below the sidewalk, which generally returns to baseline over subsequent days. The late September 2025 event sustains these elevated values longer, taking 4 days to peak in the GI and twice as long below the sidewalk (it is still returning to baseline during the event at t_5). Deeper variations below the water table remain small, not exceeding ±2%. This pattern is reflected in the time series in the first row, where fluctuations are confined to locations above the water table, including beneath the road and between the GI and the road (see the dark blue and pale purple series for t_1 and t_5), while the remaining time series show near-constant conductivity throughout the events.

The second pattern, observed during the spring and early summer events (rainfall events 2 and 3 in April and June 2025), clearly differs from the previous one, as the bulk EC distribution does not return to its pre-rain state after the event. Overall, these events show a decrease in bulk EC above the water table ranging from 4 to 16%, while a marked increase of around 10% occurs deeper in the saturated zone. This behavior ceases in late June, when relative bulk EC changes begin to resemble a combination of the two patterns described previously.

This figure provides a high-resolution temporal view of individual events but remains sparse at broader timescales. By placing these events in the context of the seasonal bulk EC variations shown in Fig. 4, it becomes apparent that the response of the GI and its surroundings to rainfall evolves throughout the year in terms of bulk EC.

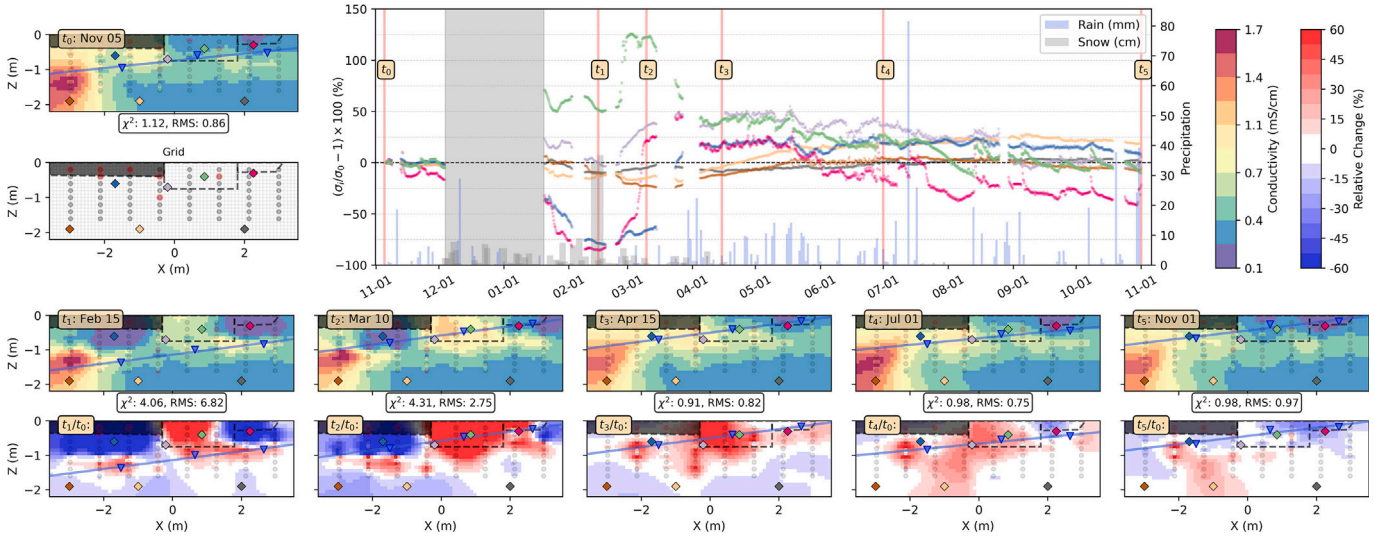


Fig. 4. Inverted and temperature-corrected bulk EC images sampled six times between November 5, 2024 (t_0) and November 1, 2025 (t_5), with the corresponding color bars in the top right. The last row shows relative changes compared to t_0. In all spatial plots, the water table level at t_i is represented by a blue line. The top wide panel displays seven time series of relative changes sampled at seven key locations (top-left blank profile), underscoring the dynamic and temporal sampling of the chosen time-steps. All models result from inversions using 118 quadrupoles. (For interpretation of the references to colour in this figure legend, the reader is referred to the web version of this article.)

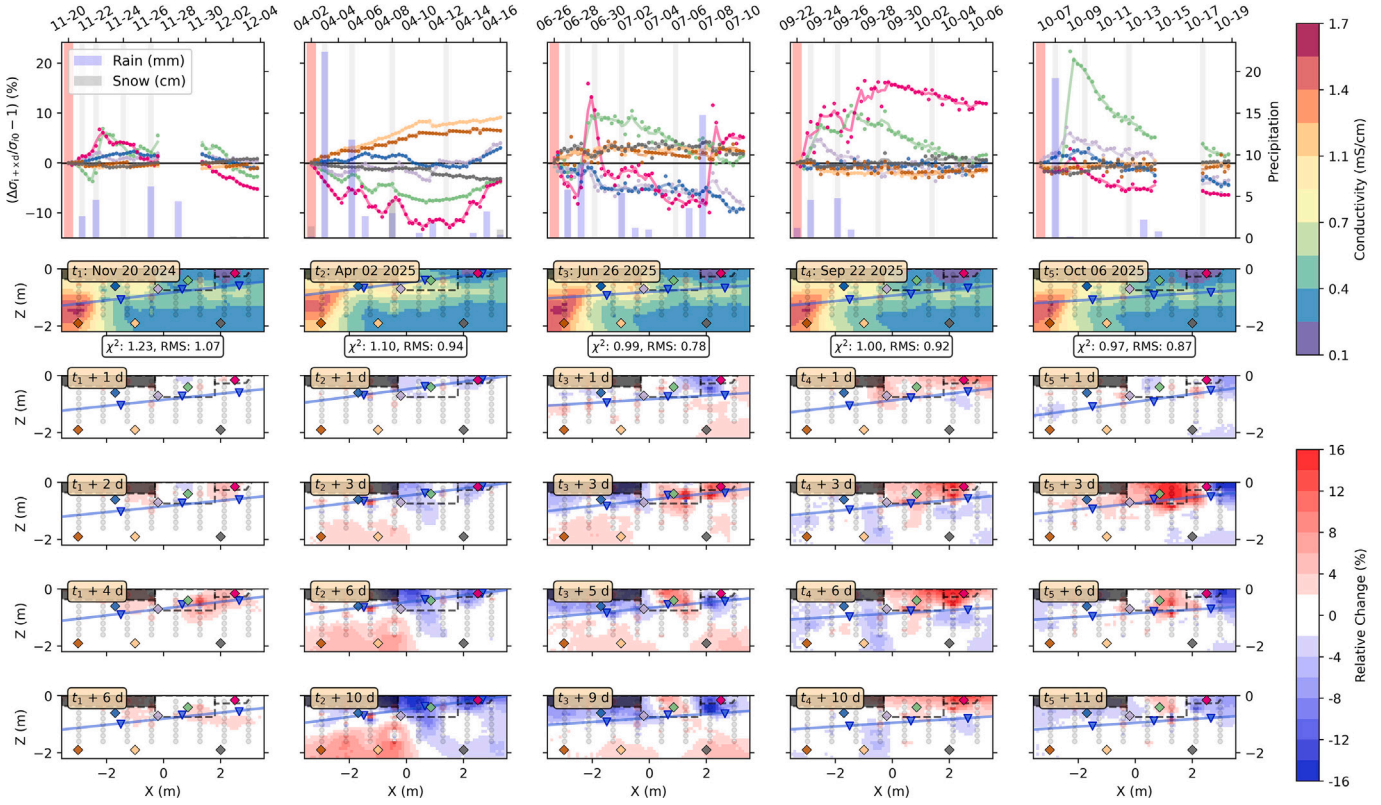


Fig. 5. The second row shows inverted and corrected bulk EC models sampled five times between November 20, 2024 (t_1) and October 5, 2025 (t_5), color bar is at the top right. Each subsequent image going downward shows the relative change in conductivity (Eq. 6) after a rain event compared to the first time step t_i. The corresponding color bar is located at the bottom right. The top panel displays time series of relative variations sampled at seven key positions in the profile (colored diamonds), further highlighting the dynamic and temporal sampling of the chosen time-steps. All 2D spatial plots show the extrapolated water table level at the time of the snapshot. All models result from inversions using 118 quadrupoles. (For interpretation of the references to colour in this figure legend, the reader is referred to the web version of this article.)

3.5. Clusters' seasonal bulk EC variations

Fig. 6 presents the mean bulk EC variations relative to November 5, 2024 (t_0), for each cluster, summarizing the temporal evolution of the profile alongside groundwater levels and daily precipitation. The time-series clustering (TSC) analysis is performed on 1562 individual cell time series derived from the 1222 inverted and temperature-corrected 2D bulk EC models. The five-cluster configuration is selected based on three criteria: alignment with the known site stratigraphy (Fig. 1), spatial coherence, and the distinctiveness of the temporal dynamics exhibited by each cluster. A six-cluster configuration was rejected as over-segmented, as the additional cluster displayed dynamics nearly identical to another one. The 5 clusters seem to correspond well to the known stratigraphy of the study site and exhibit distinct temporal behavior, both in terms of bulk EC absolute values and in terms of variations. Several other partitions with 4, 5, and 6 clusters obtained using different pre-processing methods are presented in Supplementary Figure S8.

Results reveal a clearer cyclical behavior than previously (Fig. 4), which can be divided into four distinct periods: early winter, late winter, spring, and summer/autumn. During early winter, the GI (cluster 1) exhibited a sharp 90% increase in conductivity, whereas the road and sidewalk zones (clusters 4 and 5) showed a mean decrease of approximately 40%. In late winter (late February in this case), the first rainfall events triggered a marked rise in the water table and a profile-wide conductivity spike (20% to 80%). During these periods, the lower profile showed opposing trends on the left and right, each reaching about 15% before changing trend. In spring (April–May), the first rainfall events and the warming temperatures led to a 10% to 40% decrease in the GI cluster, while the bottom left cluster (2, in purple) showed a steady upward trend. Finally, the summer/autumn period resulted in a slow 20% to 50% conductivity drop in the GI and sidewalk zones before groundwater levels and conductivity variations stabilized again in autumn.

The five clusters highlight functionally different zones. The GI and the zone below the sidewalk (clusters 1 and 5) show a response to precipitation events that evolves throughout the year, with an initially strong response following snowmelt, followed by a gradual downward trend, and a renewed sharp response beginning in late summer (see Fig. 5). The zone below the road (cluster 4) exhibits few changes outside of winter and high water table periods, while the deeper saturated zones (clusters 2 and 3) display more gradual, dampened responses. This partition provides a quantitative framework for characterizing the seasonal behavior of each hydrogeological unit, facilitating the interpretation of bulk EC variations as hydrogeochemical behaviors.

4. Discussion

4.1. Hydrogeochemical seasonal behavior of the GI

In this study, the ERT-derived conductivity distribution matched the known stratigraphy. The results show a clear cyclical pattern in bulk EC variations throughout the year. Consequently, the top profile of Fig. 3 from November 5, obtained using all electrodes with the SAS 4000, can be considered a representative background conductivity distribution. Although this study focuses on temporal dynamics, establishing such a baseline is important because it reflects longer-term processes and integrates the cumulative effects of repeated winter de-icing salt applications and residual solute storage from previous years.

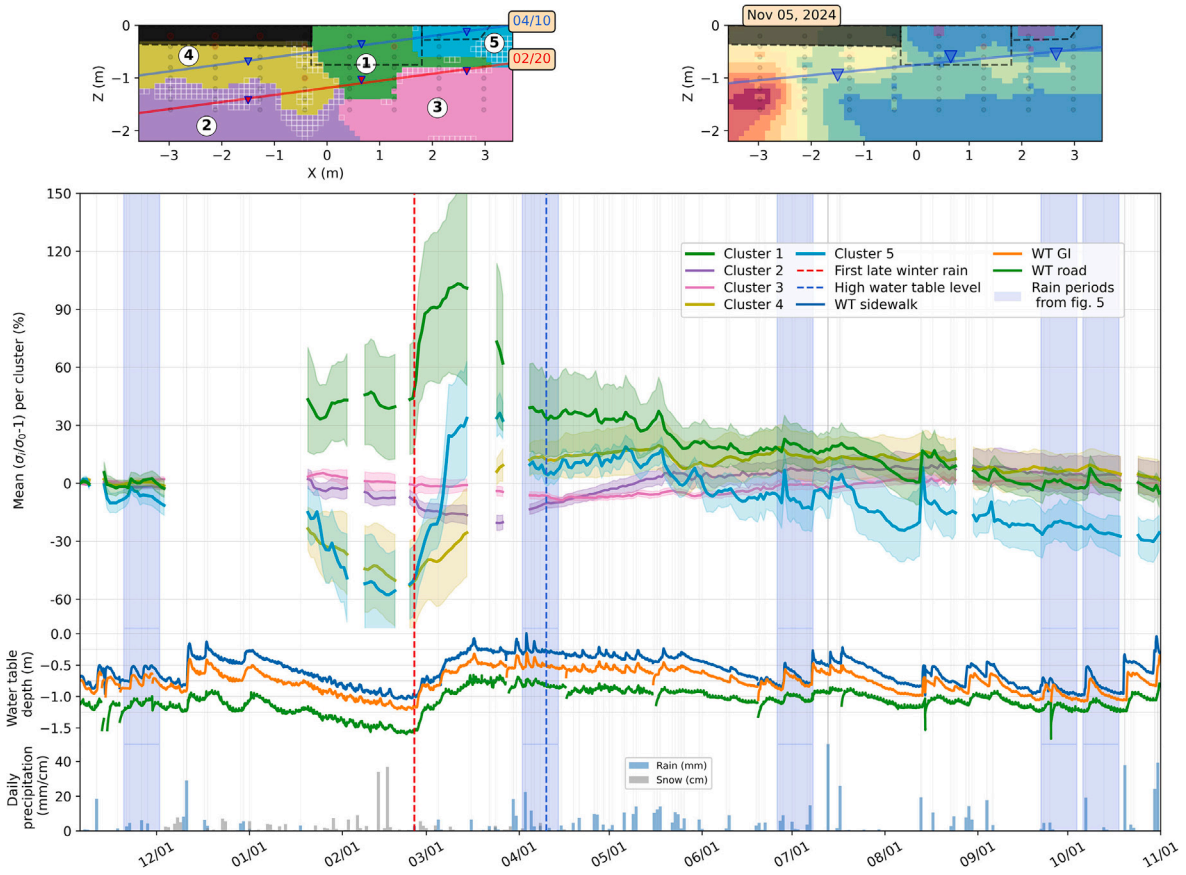


Fig. 6. The top left image shows the clustering partition obtained for five clusters. The top right image is for comparison. The bottom figure displays time series of mean bulk EC relative variations for each cluster (compared to November 5, 2024), the shaded area being the cluster's standard deviation. The blue, Orange and green plot shows water table (WT) depths measured at three locations and the last row show daily precipitation. (For interpretation of the references to colour in this figure legend, the reader is referred to the web version of this article.)

These residual effects are consistent with observations in urban GI. For instance, Pope et al. (2025) reported baseline bulk EC values increasing from 0.125–0.2 mS/cm in October to 0.4–0.66 mS/cm by February, while Hodgins et al. (2023) and Hodgins et al. (2024) observed a highly conductive zone reaching 1.2–1.5 mS/cm beneath a shallow streambed adjacent to a parking area. Although these studies did not account for temperature variations, our results show a similar post-winter increase and overall cyclic behavior as documented by Hernandez Gonzalez et al. (2023). In our case, the most conductive zone matches the observed hydraulic gradient and is consistent with the groundwater sampling results showing increasing EC and chloride concentrations toward the road side of the profile (see Supplementary Figures S9, S10 and S11). These patterns are consistent with the accumulation effects described by Kelly et al. (2008) and Szklarek et al. (2022), which contribute to the establishment of a persistent, long-term chloride baseline.

Fig. 7 presents a conceptual model of the behavior of the GI throughout the year. The first phase can be divided into three parts: early winter (onset of snowfall and road salt application), late winter (first rain events and accelerated snowmelt), and spring (increasing temperatures and frequent rainfall). In early winter, bulk EC increases at the GI surface as road salts infiltrate, while values beneath the sidewalk and road decrease due to falling water tables and reduced VWC. Surface freezing may further lower bulk EC by reducing the liquid water fraction. Simultaneously, the deeper saturated zone shows a decline in bulk EC, consistent with dilution by lower-EC groundwater and limited chloride inputs. By late winter, rain and snowmelt trigger sharp near-surface bulk EC increases as accumulated salts are mobilized, a mechanism documented by Weatherson et al. (2024). It should be noted that the previous rainfall events in December and January probably exhibited a similar dynamic but were not monitored in 2025. Infiltration observed beneath the road suggests the pavement is not entirely impermeable, which is highly likely given the longitudinal crack visible in Supplementary Figure S7. During the spring transition, sustained rainfall drives downward solute transport along the hydraulic gradient. As shown in Fig. 5, April and June events exhibit distinct flushing behaviors: the April response is consistent with a stronger influence of pore-water and surface conductivity changes, whereas the June event suggests a transition toward a greater contribution of VWC-driven bulk EC variations. However, the relative contribution of these mechanisms cannot be quantified with the available dataset. Throughout these phases, the GI delays salt transport to deeper layers, providing a buffering effect consistent with Shannon et al. (2020). As shown in Fig. 1, the GI includes an underdrain at the base of the GI. Despite its presence, the ERT results and their interpretation suggest that part of the chloride load infiltrates beyond the GI and reaches the groundwater system. Additional monitoring of underdrain discharge would help determine the proportion of chloride exported through drainage versus that reaching groundwater.

The final two models at the bottom of Fig. 7 illustrate the response of the GI to a rainfall event. Shortly after a rainfall, bulk EC increases within the GI, beneath the sidewalk, and to a lesser extent under the pavement. Water enters primarily through the curb cut, though some infiltration may also occur through the grassed area to the right of the profile. This influx triggers a shallow rise in the water table, with the magnitude dictated by rainfall intensity. Over the subsequent 4 to 8 days, bulk EC gradually decreases as the system returns to pre-rainfall conditions. This

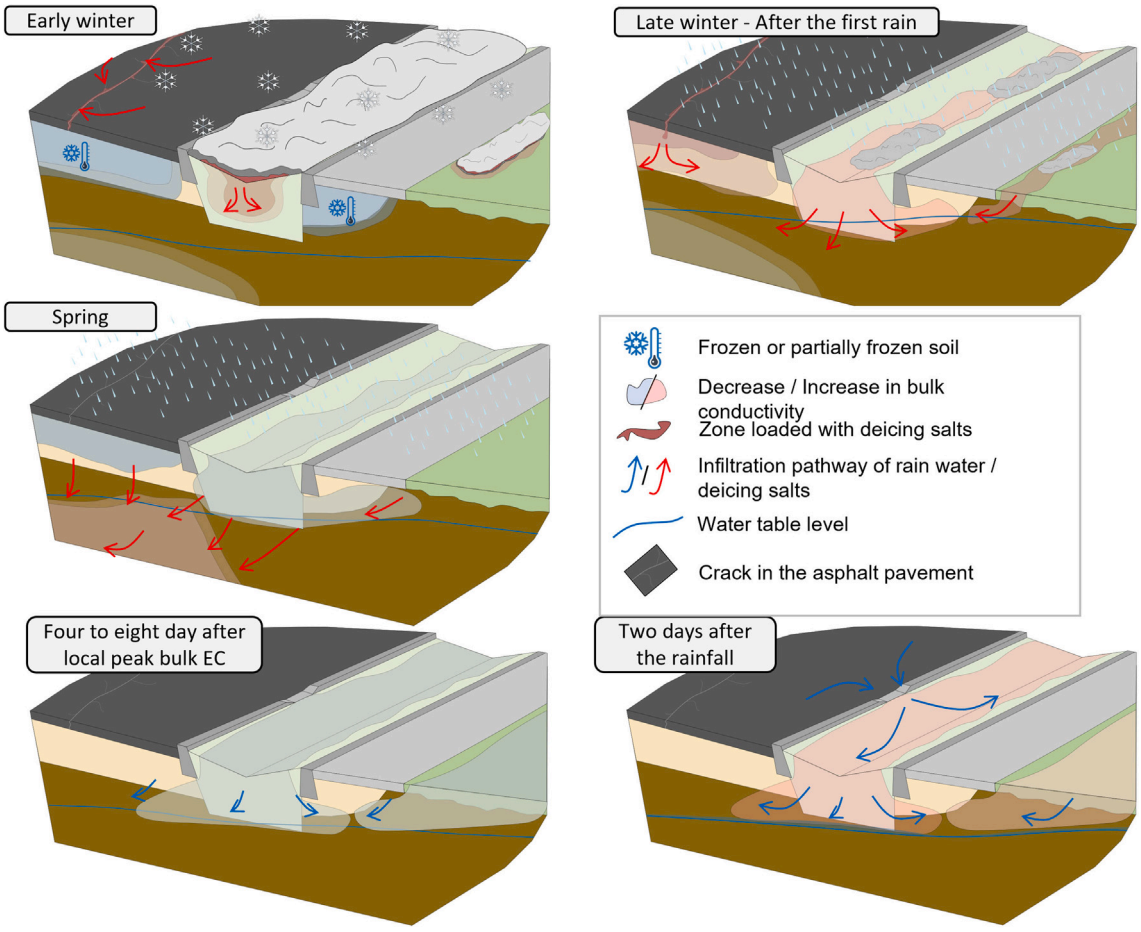


Fig. 7. Conceptual model of the winter and spring behavior of the GI and its surroundings based on empirical observations. The first row represents the 2 behaviors during the first and second halves of winter. The second row displays the following processes happening in spring. The last row shows the response to a rainfall event in late summer and autumn.

recovery suggests that variations in VWC are the primary drivers of near-surface bulk EC changes from late summer until the first snowfall. This interpretation is supported by observations during a prolonged dry period in late July, during which soil desaturation produced EC decreases of similar magnitude in both the GI and the zone below the sidewalk.

4.2. Relevance of TL-ERT and TSC in urban context

The use of cross-borehole TL-ERT represents a promising approach for studying urban GI, enabling high resolution imaging capable of detecting bulk EC variations of only a few percent over a whole profile. While recent studies have applied surface-based TL-ERT to characterize urban subsurface pathways and GI systems (Hodgins et al., 2023, 2024; Pope et al., 2025), the cross-borehole configuration used here provides substantially higher spatial resolution at this scale. The system demonstrates robustness, and inverted models remain spatially consistent and highly representative of the profile. This long-term monitoring is made possible by the recent development of open-source hardware by the OhmPi team (Clement et al., 2020; Blanchy et al., 2024), offering affordable instrumentation and underscoring the need for broader collaboration on open-source tools, whether hardware (Basson et al., 2021; Guyard et al., 2025) or software (Heagy et al., 2024). The TSC method acts as a relevant tool to support the hydrogeochemical interpretation of the geophysical dataset. By clustering cells based on temporal correlation, TSC reduces thousands of time series to a few distinct units, enabling continuous evaluation of pseudo-spatial trends across timescales.

4.3. Limitations of the method and recommendations for further characterization

To enable a more precise evaluation of bulk EC variations and to produce quantitative estimations of pore water conductivity or VWC, as demonstrated by Dimech et al. (2024) and Grünenbaum et al. (2023), more advanced approaches could be implemented. For instance, adaptive measurement protocols, as proposed by Slater and Binley (2021) and Wilkinson et al. (2015), could improve the synchronization between hydrogeological processes and conductivity imaging. In addition, optimized acquisition strategies (Uhlemann et al., 2018; Qiang et al., 2022) could compensate for unusable electrodes by locally adapting measurement configurations. A more thorough evaluation of potential borehole fluid effects (Doetsch et al., 2010) would also be beneficial, as artifacts appear in several ratio images (e.g., Fig. 4). These could potentially be mitigated using the updated inversion method described in Lee et al. (2016).

Furthermore, vertical temperature models (e.g., Eq. 3) indicate that soil temperatures fall below 0 °C at a 60 cm depth during winter (January–March) beneath the road and sidewalk, whereas the GI reaches sub-zero temperatures only in February, likely due to the insulating effect of the snow pile. These conditions suggest the presence of frozen or partially frozen soils within the monitored profile, consistent with conductivity data indicating partially frozen soil even near the surface. Temperature correction methods accounting for partially frozen soils (Herring et al., 2021) could improve the evaluation of winter near-surface conductivity. Applying temperature corrections directly to raw

measurements (Hayley et al., 2010) could further enhance the results, as differences in vertical temperature profiles may propagate through temperature extrapolation and inversion smoothing. More broadly, temperature correction remains challenging because the electrical response to temperature varies with local hydrogeological conditions, including stratigraphy and groundwater level, making it difficult to separate thermal effects from true hydrogeochemical changes (Xia et al., 2026a).

In the context of the TSC method, our final choice of partition is heavily driven by its alignment with the known subsurface geometry, which introduces a degree of subjectivity and contradicts the supposedly objective, data-driven nature of clustering algorithms. The resulting partition was not entirely stable: changes in the dataset or preprocessing could lead to different outcomes. Although the GI and the sidewalk are well identified most of the time, deeper regions often result in less consistent clusters. To mitigate this in future studies and obtain a partition that is purely representative of the dataset's intrinsic structure, an approach using consensus clustering (Monti et al., 2003), as suggested by Delforge et al. (2021), could be implemented. This would provide a more robust and rigorous basis for extracting bulk EC dynamics from large TL-ERT datasets without relying on prior structural assumptions.

A major next step toward improving our understanding of subsurface processes is the integration of TL-ERT observations with multiphysics modeling (Wagner and Uhlemann, 2021; Moorkamp et al., 2016). Such an approach would enable the estimation of hydrogeologically relevant parameters rather than geophysical properties alone (Hermans et al., 2023). For example, petrophysically and geologically guided multiphysics inversion (Astic et al., 2020), as well as Bayesian evidential learning approaches for characterizing contaminant pathways (Miao et al., 2026), could provide robust in situ estimates of key subsurface properties and hydrogeological processes that remain difficult to constrain using conventional methods, particularly in heterogeneous urban environments. Ultimately, even the most sophisticated processing schemes should not rely on geophysical data alone. As Herweijer et al. (2026) notes, advanced interpretive methods must always incorporate available complementary information, and a cross-validation scheme successfully applied by Xia et al. (2026b).

5. Conclusion

In this study, cross-borehole TL-ERT is combined with TSC to investigate subsurface processes in an urban environment. A roadside GI installation and its surroundings are instrumented with a high-density cross-borehole ERT array and complementary hydrogeological sensors. Autonomous geoelectrical monitoring was conducted over more than one year, capturing both seasonal and event-scale dynamics that are rarely observable using conventional approaches.

The results revealed pronounced seasonal patterns, notably rapid conductivity changes during spring snowmelt, interpreted as chloride migration associated with de-icing salt inputs. The monitoring demonstrates the capability of TL-ERT to efficiently resolve small-scale subsurface conductivity variations at high spatial and temporal resolution in a geometrically complex and heterogeneous urban setting. Time-series clustering of resistivity data proved effective in discriminating distinct hydrogeological behaviors within the subsurface, highlighting contrasts in infiltration and solute transport that would be difficult to identify using point-based measurements alone.

These findings have important implications for urban water management and infrastructure design. The proposed approach provides empirical, spatially distributed data that can support the evaluation, validation, and optimization of GI performance under real operating conditions. In addition, the resulting dataset offers a valuable basis for calibrating and constraining hydrological, hydrogeological, and solute-transport models in urban environments.

Several limitations should be acknowledged. Temperature correction of bulk EC remains challenging in partially frozen soil, precipitation was not directly monitored on site, and the use of open-source hardware exhibited reduced performance in coarse, crushed-stone materials. These factors introduce uncertainties that should be addressed in future deployments. Future work will focus on improving ERT monitoring strategies and coupling geophysical observations with numerical modeling constrained by conductivity data and laboratory-based petrophysical characterization.

In conclusion, autonomous and low-cost geophysical monitoring represents a promising and accessible approach for improving the understanding of urban subsurface processes, supporting infrastructure design decisions, and fostering more resilient urban systems grounded in robust empirical evidence.

CRediT authorship contribution statement

Alexis Luzy: Writing – review & editing, Writing – original draft, Visualization, Validation, Resources, Methodology, Investigation, Formal analysis, Data curation. **Adrien Dimech:** Writing – review & editing, Visualization, Validation, Supervision, Resources, Project administration, Methodology, Investigation, Funding acquisition, Conceptualization. **François Duhaime:** Writing – review & editing, Validation, Supervision, Resources, Project administration, Methodology, Investigation, Funding acquisition, Conceptualization. **Janie Masse-Dufresne:** Writing – review & editing, Validation, Resources, Investigation, Funding acquisition, Conceptualization. **Jean-Sébastien Dubé:** Writing – review & editing, Validation, Resources, Investigation, Funding acquisition, Conceptualization. **Rose-Anne Farley:** Writing – review & editing, Visualization, Validation, Resources, Investigation, Formal analysis. **Rémi Clément:** Writing – review & editing, Validation. **Maxime Paradis:** Resources, Project administration, Funding acquisition.

Declaration of competing interest

The authors declare that they have no known competing financial interests or personal relationships that could have appeared to influence the work reported in this paper.

Acknowledgements

This work was made possible through the collaboration and financial support of the City of Laval, the City of Montreal, Mitacs (grant number ALLRP 588361-23), and the CRSNG. Their combined commitment to research, innovation, and partnership was instrumental in supporting the development and successful completion of this project.

Appendix A. Supplementary data

Supplementary data for this article can be found online at doi:10.1016/j.jhydrol.2026.136632.

Data availability

Data will be made available on request.

References

Abraham, A., Pedregosa, F., Eickenberg, M., Gervais, P., Mueller, A., Kossaifi, J., Gramfort, A., Thirion, B., Varoquaux, G., 2014. Machine learning for neuroimaging with Scikit-Learn. Front. Neuroinformatics 8, https://doi.org/10.3389/fninf.2014.00014. http://journal.frontiersin.org/article/10.3389/fninf.2014.00014/abstract.

Aghabozorgi, S., Seyed Shirkhorshidi, A., Ying Wah, T., 2015. Time-series clustering – a decade review. Inf. Syst. 53, 16–38. https://doi.org/10.1016/j.is.2015.04.007. https://linkinghub.elsevier.com/retrieve/pii/S0306437915000733.

Astic, T., Heagy, L.J., Oldenburg, D.W., 2020. Petrophysically and geologically guided multi-physics inversion using a dynamic Gaussian mixture model. Geophys. J. Int. 224, 40–68. https://doi.org/10.1093/gji/ggaa378. https://academic.oup.com/gji/article/224/1/40/5895341.

BAC, 2024. Événement météorologique le plus coûteux de l'histoire du Québec: les inondations d'août causent près de 2, 5 milliards de dollars de dommages assurés. https://bac-quebec.qc.ca/media/kozngael/nr-2024-09-10-qc_flooding_estimates_sept4-24_v04_pb_fr.pdf.

Basson, J.A., Broekman, A., Jacobsz, S.W., 2021. TD-DAQ: a low-cost data acquisition system monitoring the unsaturated pore pressure regime in tailings dams. HardwareX 10, e00221. https://doi.org/10.1016/j.ohx.2021.e00221. https://linkinghub.elsevier.com/retrieve/pii/S246806722100050X.

Beral, H., Dagenais, D., Brisson, J., Kõiv-Vainik, M., 2023. Impact of de-icing Salt runoff in spring on bioretention efficiency. Blue-Green Syst. 5, 170–185. https://doi.org/10.2166/bgs.2023.036. https://iwaponline.com/bgs/article/5/2/170/98569/Impact-of-de-icing-salt-runoff-in-spring-on.

Bhaskar, A.S., Beesley, L., Burns, M.J., Fletcher, T.D., Hamel, P., Oldham, C.E., Roy, A.H., 2016. Will it rise or will it fall? Managing the complex effects of urbanization on base flow. Freshw. Sci. 35, 293–310. https://doi.org/10.1086/685084

Blanchy, G., Watlet, A., Clément, R., Kaufmann, O., Forquet, N., Guyard, H., 2024. OhmPi: learn how to build an open-source resistivity meter. In: Agriculture and Geophysics: Illuminating the Subsurface. Agrogeophysics, pp. 33, https://doi.org/10.62329/MCKV3023

Bonneau, J., Fletcher, T.D., Costelloe, J.F., Poelsma, P.J., James, R.B., Burns, M.J., 2018. Where does infiltrated stormwater go? Interactions with vegetation and subsurface anthropogenic features. J. Hydrol. 567, 121–132. https://doi.org/10.1016/j.jhydrol.2018.10.006. https://linkinghub.elsevier.com/retrieve/pii/S0022169418307674.

Botturi, A., Ozbayram, E.G., Tondera, K., Gilbert, N.I., Rouault, P., Caradot, N., Gutierrez, O., Daneshgar, S., Frison, N., Akyol Foglia, A., Eusebi, A.L., Fatone, F., 2021. Combined sewer overflows: a critical review on best practice and innovative solutions to mitigate impacts on environment and human health. Crit. Rev. Environ. Sci. Technol. 51, 1585–1618. https://doi.org/10.1080/10643389.2020.1757957

Brunet, P., Clément, R., Bouvier, C., 2010. Monitoring soil water content and deficit using electrical resistivity tomography (ERT) – a case study in the cevennes area, France. J. Hydrol. 380, 146–153. https://doi.org/10.1016/j.jhydrol.2009.10.032. https://linkinghub.elsevier.com/retrieve/pii/S002216940900691X.

Burgis, C.R., Hayes, G.M., Henderson, D.A., Zhang, W., Smith, J.A., 2020. Green stormwater infrastructure redirects deicing Salt from surface water to groundwater. Sci. Total Environ. 729, 138736. https://doi.org/10.1016/j.scitotenv.2020.138736. https://linkinghub.elsevier.com/retrieve/pii/S0048969720322531.

Chambers, J., Gunn, D., Wilkinson, P., Meldrum, P., Haslam, E., Holyoake, S., Kirkham, M., Kuras, O., Merritt, A., Wragg, J., 2014. 4D electrical resistivity tomography monitoring of soil moisture dynamics in an operational railway embankment. Near Surf. Geophys. 12, 61–72. https://doi.org/10.3997/1873-0604.2013002

Chapuis, R.P., 1999. Guide Des Essais de Pompage Et Leurs Interprétations. Technical Report, Service de L'aménagement Et Des Eaux Souterraines Du Ministère Du Développement Durable, de L'Environnement Et Des Parcs.

Chen, S., Qin, H.P., Zheng, Y., Fu, G., 2019. Spatial variations of pollutants from sewer interception system overflow. J. Environ. Manag. 233, 748–756. https://doi.org/10.1016/j.jenvman.2018.09.082. https://linkinghub.elsevier.com/retrieve/pii/S0301479718310922.

Clément, R., Moreau, S., Henine, H., Guérin, A., Chaumont, C., Tournebize, J., 2014. On the value of combining surface and cross-borehole ERT measurements to study artificial tile drainage processes. Near Surf. Geophys. 12, 763–776. https://doi.org/10.3997/1873-0604.2014034

Clement, R., Fargier, Y., Dubois, V., Gance, J., Gros, E., Forquet, N., 2020. OhmPi: an open source data logger for dedicated applications of electrical resistivity imaging at the small and laboratory scale. HardwareX 8, e00122. https://doi.org/10.1016/j.ohx.2020.e00122. https://linkinghub.elsevier.com/retrieve/pii/S2468067220300316.

Corsi, S.R., Graczyk, D.J., Geis, S.W., Booth, N.L., Richards, K.D., 2010. A fresh look at road Salt: aquatic toxicity and water-quality impacts on local, regional, and national scales. Environ. Sci. Technol. 44, 7376–7382. https://doi.org/10.1021/es101333u

Deeb, M., Groffman, P.M., Blouin, M., Egendorf, S.P., Vergnes, A., Vasenev, V., Cao, D.L., Walsh, D., Morin, T., Séré, G., 2020. Using constructed soils for green infrastructure – challenges and limitations. SOIL 6, 413–434. https://doi.org/10.5194/soil-6-413-2020. https://soil.copernicus.org/articles/6/413/2020/.

Delforge, D., Watlet, A., Kaufmann, O., Van Camp, M., Vanclooster, M., 2021. Time-series clustering approaches for subsurface zonation and hydrofacies detection using a real time-lapse electrical resistivity dataset. J. Appl. Geophys. 184, 104203. https://doi.org/10.1016/j.jappgeo.2020.104203. https://linkinghub.elsevier.com/retrieve/pii/S0926985120305863.

Denich, C., Bradford, A., Drake, J., 2013. Bioretention: assessing effects of winter Salt and aggregate application on plant health, media clogging and effluent quality. Water Qual. Res. J. 48, 387–399. https://doi.org/10.2166/wqrjc.2013.065

Dimech, A., Cheng, L., Chouteau, M., Chambers, J., Uhlemann, S., Wilkinson, P., Meldrum, P., Mary, B., Fabien-Ouellet, G., Isabelle, A., 2022. A review on applications of time-lapse electrical resistivity tomography over the last 30 years: perspectives for mining waste monitoring. Surv. Geophys. 43, 1699–1759. https://doi.org/10.1007/s10712-022-09731-2

Dimech, A., Isabelle, A., Sylvain, K., Liu, C., Cheng, L., Bussière, B., Chouteau, M., Fabien-Ouellet, G., Bérubé, C., Wilkinson, P., Meldrum, P., Chambers, J., 2023. A multiscale accuracy assessment of moisture content predictions using time-lapse electrical resistivity tomography in mine tailings. Sci. Rep. 13, 20922. https://doi.org/10.1038/s41598-023-48100-w. https://www.nature.com/articles/s41598-023-48100-w.

Dimech, A., Bussière, B., Cheng, L., Chouteau, M., Fabien-Ouellet, G., Chevé, N., Isabelle, A., Wilkinson, P., Meldrum, P., Chambers, J., 2024. Monitoring moisture dynamics in multi-layer cover systems for mine tailings reclamation using autonomous and remote time-lapse electrical resistivity tomography. Can. Geotech. J. 61, 2505–2522. https://doi.org/10.1139/cgj-2023-0112

Doetsch, J.A., Coscia, I., Greenhalgh, S., Linde, N., Green, A., Günther, T., 2010. The borehole-fluid effect in electrical resistivity imaging. Geophysics 75, F107–F114. https://doi.org/10.1190/1.3467824. https://pubs.geoscienceworld.org/geophysics/article/75/4/F107/303127/The-borehole-fluid-effect-in-electrical.

Dugué, M., 2022. Guide de conception GCI-3A infrastructures vertes sur rue avec infiltration complète. https://ville.montreal.qc.ca/executiontravaux/document/gci-3a.

Fares, A., Deb, S.K., Fares, S., 2009. Review of vadose zone soil solution sampling techniques. Environ. Rev. 17, 215–234. https://doi.org/10.1139/A09-010

Fletcher, T.D., Shuster, W., Hunt, W.F., Ashley, R., Butler, D., Arthur, S., Trowsdale, S., Barraud, S., Semadeni-Davies, A., Bertrand-Krajewski, J.L., Mikkelsen, P.S., Rivard, G., Uhl, M., Dagenais, D., Viklander, M., 2015. SUDS, LID, BMPs, WSUD and more – the evolution and application of terminology surrounding urban drainage. Urban Water J. 12, 525–542. https://doi.org/10.1080/1573062X.2014.916314

Gogien, F., Dechesne, M., Martinerie, R., Lipeme Kouyi, G., 2023. Assessing the impact of climate change on combined sewer overflows based on small time step future rainfall timeseries and long-term continuous sewer network modelling. Water Res. 230, 119504. https://doi.org/10.1016/j.watres.2022.119504. https://linkinghub.elsevier.com/retrieve/pii/S004313542201449X.

Gooré Bi, E., Monette, F., Gasperi, J., Perrodin, Y., 2015. Assessment of the ecotoxicological risk of combined sewer overflows for an aquatic system using a coupled "substance and bioassay" approach. Environ. Sci. Pollut. Res. 22, 4460–4474. https://doi.org/10.1007/s11356-014-3650-9

Grünenbaum, N., Günther, T., Greskowiak, J., Vienken, T., Müller-Petke, M., Massmann, G., 2023. Salinity distribution in the subterranean estuary of a meso-tidal high-energy beach characterized by electrical resistivity tomography and direct push technology. J. Hydrol. 617, 129074. https://doi.org/10.1016/j.jhydrol.2023.129074. https://linkinghub.elsevier.com/retrieve/pii/S0022169423000161.

Guyard, H., Prost-Boucle, S., Sudre, J., Moreau, S., Imig, A., Favreau, G., Quatela, V., Clement, R., 2025. An open source ultrasonic flowmeter for monitoring the input/output flow rates of wastewater treatment plants. HardwareX 21, e00613. https://doi.org/10.1016/j.ohx.2024.e00613. https://linkinghub.elsevier.com/retrieve/pii/S246806722400107X.

Hayley, K., Bentley, L.R., Gharibi, M., Nightingale, M., 2007. Low temperature dependence of electrical resistivity: implications for near surface geophysical monitoring. Geophys. Res. Lett. 34, 2007GL031124. https://doi.org/10.1029/2007GL031124

Hayley, K., Bentley, L.R., Pidlisecky, A., 2010. Compensating for temperature variations in time-lapse electrical resistivity difference imaging. Geophysics 75, WA51–WA59. https://doi.org/10.1190/1.3478208

Heagy, L.J., Kang, S., Capriotti, J., Fournier, D., Cockett, R., Oldenburg, D.W., 2024. Opportunities for open-source software to accelerate research in applied geophysics. Lead. Edge 43, 84–94. https://doi.org/10.1190/tle43020084.1. https://pubs.geoscienceworld.org/tle/article/43/2/84/633846/Opportunities-for-open-source-software-to.

Hermans, T., Goderniaux, P., Jougnot, D., Fleckenstein, J.H., Brunner, P., Nguyen, F., Linde, N., Huisman, J.A., Bour, O., Lopez Alvis, J., Hoffmann, R., Palacios, A., Cooke, A.K., Pardo-Álvarez, Blazevic, L., Pouladi, B., Haruzi, P., Fernandez Visentini, A., Nogueira, G.E.H., Tirado-Conde, J., Looms, M.C., Kenshilikova, M., Davy, P., Le Borgne, T., 2023. Advancing measurements and representations of subsurface heterogeneity and dynamic processes: towards 4D hydrogeology. Hydrol. Earth Syst. Sci. 27, 255–287. https://doi.org/10.5194/hess-27-255-2023. https://hess.copernicus.org/articles/27/255/2023/.

Hernandez Gonzalez, L.M., Rivera, V.A., Akosa, D., Phillips, C.B., Hatch, S.L., Miller, W.M., Packman, A.I., 2023. Road Salt intrusion dynamics in an ex-urban native wetland complex. PLOS Water 2, e0000148. https://doi.org/10.1371/journal.pwat.0000148

Herring, T., Pidlisecky, A., Cey, E., 2021. Removing the effects of temperature on electrical resistivity tomography data collected in partially frozen ground: limitations and considerations for field applications. Vadose Zone J. 20, e20146. https://doi.org/10.1002/vzj2.20146

Herweijer, J.C., Young, S.C., Hayes, P., Batelaan, O., 2026. A multi-conceptual model approach to untangling the MADE experiment. Groundwater 64, 130–147. https://doi.org/10.1111/gwat.70049

Hodgins, G., Robinson, C.E., Roy, J.W., Power, C., 2023. Characterization of subsurface pathways contributing to freshwater salinization of urban streams using electrical and electromagnetic imaging techniques. Sci. Total Environ. 905, 167225. https://doi.org/10.1016/j.scitotenv.2023.167225. https://linkinghub.elsevier.com/retrieve/pii/S0048969723058527.

Hodgins, G., Robinson, C.E., Power, C., Roy, J.W., 2024. Road Salt chloride exposure in urban streambeds and links to groundwater – surface water interactions and Salt sources. Sci. Total Environ. 957, 177488. https://doi.org/10.1016/j.scitotenv.2024.177488. https://linkinghub.elsevier.com/retrieve/pii/S0048969724076459.

Ingeman-Nielsen, T., Tomaškovičová, S., Dahlin, T., 2016. Effect of electrode shape on grounding resistances — Part 1: The focus-one protocol. Geophysics 81, WA159–WA167. https://doi.org/10.1190/geo2015-0484.1

Jain, A.K., Murty, M.N., Flynn, P.J., 1999. Data clustering: a review. ACM Comput. Surv. 31, 264–323. https://doi.org/10.1145/331499.331504

Jean, M., Morin, C., Duchesne, S., Pelletier, G., Pleau, M., 2021. Optimization of real-time control with green and gray infrastructure design for a cost-effective mitigation of combined sewer overflows. Water Resour. Res. 57, e2021WR030282. https://doi.org/10.1029/2021WR030282

Jean, M., Morin, C., Duchesne, S., Pelletier, G., Pleau, M., 2022. Real-time model predictive and rule-based control with green infrastructures to reduce combined sewer overflows. Water Res. 221, 118753. https://doi.org/10.1016/j.watres.2022.118753. https://linkinghub.elsevier.com/retrieve/pii/S0043135422007060.

Jordi, C., Doetsch, J., Günther, T., Schmelzbach, C., Robertsson, J.O., 2018. Geostatistical regularization operators for geophysical inverse problems on irregular meshes. Geophys. J. Int. 213, 1374–1386. https://doi.org/10.1093/gji/ggy055. https://academic.oup.com/gji/article/213/2/1374/4847897.

Kaushal, S.S., Belt, K.T., 2012. The urban watershed continuum: evolving spatial and temporal dimensions. Urban Ecosyst. 15, 409–435. https://doi.org/10.1007/s11252-012-0226-7

Kelly, V.R., Lovett, G.M., Weathers, K.C., Findlay, S.E.G., Strayer, D.L., Burns, D.J., Likens, G.E., 2008. Long-term sodium chloride retention in a rural watershed: legacy effects of road Salt on streamwater concentration. Environ. Sci. Technol. 42, 410–415. https://doi.org/10.1021/es071391l

Kuras, O., Pritchard, J.D., Meldrum, P.I., Chambers, J.E., Wilkinson, P.B., Ogilvy, R.D., Wealthall, G.P., 2009. Monitoring hydraulic processes with automated time-lapse electrical resistivity tomography (ALERT). C. R. Géoscience 341, 868–885. https://doi.org/10.1016/j.crte.2009.07.010. https://comptes-rendus.academie-sciences.fr/geoscience/articles/10.1016/j.crte.2009.07.010/.

Kwak, N., Smith, V., Good, K.D., 2024. Assessing the influence of green stormwater infrastructure implemented for combined sewer overflow control on urban stream-flows. J. Hydrol. 640, 131670. https://doi.org/10.1016/j.jhydrol.2024.131670. https://linkinghub.elsevier.com/retrieve/pii/S0022169424010667.

LaBrecque, D.J., Miletto, M., Daily, W., Ramirez, A., Owen, E., 1996. The effects of noise on occam's inversion of resistivity tomography data. Geophysics 61, 538–548. https://doi.org/10.1190/1.1443980

Le Gigan, A., Leclerc, A., Martel, J.L., Dugué, M., Beaudry, D., Abdeljelil, I., Bérard, S., 2025. A comprehensive inspection protocol to assess stormwater green infrastructure hydraulic performance: a case study for the city of Montreal. In: Azimi, A.H., Robinson, C. (Eds.), Proceedings of the Canadian Society for Civil Engineering Annual Conference 2024, 9. Springer Nature Switzerland, Cham, pp. 253–257.

Lee, K.S., Cho, I.K., Kim, Y.J., 2016. Borehole effect in 2.5D crosshole resistivity tomography. J. Appl. Geophys. 135, 212–222. https://doi.org/10.1016/j.jappgeo.2016.10.015. https://linkinghub.elsevier.com/retrieve/pii/S0926985116304153.

Loke, M., Dahlin, T., Rucker, D.F., 2014. Smoothness-constrained time-lapse inversion of data from 3D resistivity surveys. Near Surf. Geophys. 12, 5–24. https://doi.org/10.3997/1873-0604.2013025. https://onlinelibrary.wiley.com/doi/abs/10.3997/1873-0604.2013025.

Luzy, A., Dimech, A., Duhaime, F., Dubé, J.S., Masse-Dufresne, J., 2024. Study of the hydrogeological behavior of a draining green infrastructure using continuous, high-resolution electrical resistivity tomography imaging. https://www.researchgate.net/publication/384152245_Study_of_the_hydrogeological_behavior_of_a_draining_green_infrastructure_using_continuous_high-resolution_electrical_resistivity_tomography_imaging.

Ma, R., McBratney, A., Whelan, B., Minasny, B., Short, M., 2011. Comparing temperature correction models for soil electrical conductivity measurement. Precis. Agric. 12, 55–66. https://doi.org/10.1007/s11119-009-9156-7

Mackie, C., Lackey, R., Levison, J., Rodrigues, L., 2022. Groundwater as a source and pathway for road Salt contamination of surface water in the lake Ontario basin: a review. J. Gt. Lakes Res. 48, 24–36. https://doi.org/10.1016/j.jglr.2021.11.015. https://linkinghub.elsevier.com/retrieve/pii/S0380133021002860.

Madoux-Humery, A.S., Dorner, S., Sauvé, S., Aboulfadl, K., Galarneau, M., Servais, P., Prévost, M., 2013. Temporal variability of combined sewer overflow contaminants: evaluation of wastewater micropollutants as tracers of fecal contamination. Water Res. 47, 4370–4382. https://doi.org/10.1016/j.watres.2013.04.030. https://linkinghub.elsevier.com/retrieve/pii/S004313541300359X.

Mailhot, A., Talbot, G., Lavallée, B., 2015. Relationships between rainfall and combined sewer overflow (CSO) occurrences. J. Hydrol. 523, 602–609. https://doi.org/10.1016/j.jhydrol.2015.01.063. https://linkinghub.elsevier.com/retrieve/pii/S0022169415000803.

Mason, B.E., Schmidt, J., Kerkez, B., 2023. Measuring city-scale green infrastructure drawdown dynamics using internet-connected sensors in Detroit. https://doi.org/10.48550/arXiv.2302.10969. arXiv:2302.10969.

Mayer, T., Snodgrass, W., Morin, D., 1999. Spatial characterization of the occurrence of road salts and their environmental concentrations as chlorides in Canadian surface waters and benthic sediments. Water Qual. Res. J. 34, 545–574.

Melccfp (Ed.), 2023. Guide de Gestion Des Débordements Et Des Dérivations D'eaux Usées - Tome III - Mesures de Gestion. Environnement, Lutte Contre Les Changements Climatiques, Faune Et Parcs Québec, Québec. OCLC: 1439272285.

Miao, K., Huang, Y., Zhang, L., Guo, L., Fu, Z., Hermans, T., 2026. Uncertainty analysis of contaminant sources in fracture networks: a framework integrating falsification and Bayesian evidential learning. Adv. Water Resour. 211, 105238. https://doi.org/10.1016/j.advwatres.2026.105238. https://linkinghub.elsevier.com/retrieve/pii/S0309170826000345.

Mikkelsen, P.E., 2002. Cement-Bentonite Grout Backfill for Borehole Instruments. Geotechnical Instrumentation News.

Monti, S., Tamayo, P., Mesirov, J., Golub, T., 2003. Consensus clustering: a resampling-based method for class discovery and visualization of gene expression microarray data. Mach. Learn. 52 (2003), 91–118. https://doi.org/10.1023/A:1023949509487. https://link.springer.com/content/pdf/10.1023/A:1023949509487.pdf.

Moorkamp, M., Lelièvre, P.G., Linde, N., Khan, A. (Eds.), 2016. Integrated Imaging of the Earth: Theory and Applications. Number 218 in Geophysical monograph, AGU, American Geophysical Union, Washington, DC, https://doi.org/10.1002/9781118929063

Nodine, T.G., Conley, G., Riihimaki, C.A., Holland, C., Beck, N.G., 2024. Modeling the impact of future rainfall changes on the effectiveness of urban stormwater control measures. Sci. Rep. 14, 4082. https://doi.org/10.1038/s41598-024-53611-1. https://www.nature.com/articles/s41598-024-53611-1.

O'brien, C.M., Mossman, M., Chamberlain, L., Jenkins, J., Watson, J., Wilson, R., Williams-Clark, D., Singer, A., Riggio, K., Gallet, D., Miller, W.M., Packman, A.I., 2024. Community-centered instrumentation and monitoring of nature-based solutions for urban stormwater control. Front. Water 6, 1370501. https://doi.org/10.3389/frwa.2024.1370501. https://www.frontiersin.org/articles/10.3389/frwa.2024.1370501/full.

Oladeji, E., Parsekian, A., Grana, D., 2024. Machine learning-based hydrofacies classification: effects of noise and regularization. J. Geophys. Res. Mach. Learn. Comput. 1, e2024JH000197. https://doi.org/10.1029/2024JH000197

Olds, H.T., Corsi, S.R., Dila, D.K., Halmo, K.M., Bootsma, M.J., McLellan, S.L., 2018. High levels of sewage contamination released from urban areas after storm events: a quantitative survey with sewage specific bacterial indicators. PLOS Med. 15, e1002614. https://doi.org/10.1371/journal.pmed.1002614

Parasnis, D., 1988. Reciprocity theorems in geoelectric and geoelectromagnetic work. Geoexploration 25, 177–198. https://doi.org/10.1016/0016-7142(88)90014-2. https://linkinghub.elsevier.com/retrieve/pii/0016714288900142.

Paus, K.H., Morgan, J., Gulliver, J.S., Leiknes, T., Hozalski, R.M., 2014. Assessment of the hydraulic and toxic metal removal capacities of bioretention cells after 2 to 8 years of service. Water Air Soil Pollut. 225, 1803. https://doi.org/10.1007/s11270-013-1803-y

Pedregosa, F., Varoquaux, G., Gramfort, A., Michel, V., Thirion, B., Grisel, O., Blondel, M., Prettenhofer, P., Weiss, R., Dubourg, V., Vanderplas, J., Passos, A., Cournapeau, D., 2011. Scikit-Learn: machine learning in Python. J. Mach. Learn. Res. 12 (85), 2825–2830. https://jmlr.org/papers/v12/pedregosa11a.html.

Perri, M., Cassiani, G., Gervasio, I., Deiana, R., Binley, A., 2012. A saline tracer test monitored via both surface and cross-borehole electrical resistivity tomography: comparison of time-lapse results. J. Appl. Geophys. 79, 6–16. https://doi.org/10.1016/j.jappgeo.2011.12.011. https://linkinghub.elsevier.com/retrieve/pii/S0926985111002928.

Perry, W.B., Ahmadian, R., Munday, M., Jones, O., Ormerod, S.J., Durance, I., 2024. Addressing the challenges of combined sewer overflows. Environ. Pollut. 343, 123225. https://doi.org/10.1016/j.envpol.2023.123225. https://linkinghub.elsevier.com/retrieve/pii/S0269749123022273.

Pieper, K.J., Tang, M., Jones, C.N., Weiss, S., Greene, A., Mohsin, H., Parks, J., Edwards, M.A., 2018. Impact of road Salt on drinking water quality and infrastructure corrosion in private wells. Environ. Sci. Technol. 52, 14078–14087. https://doi.org/10.1021/acs.est.8b04709

Pope, G.G., Toran, L., Caplan, J.S., Nyquist, J., 2025. Spatiotemporal dynamics of road Salt in a highway bioswale: a comparison of point and continuous monitoring methods. Water Air Soil Pollut. 236, 654. https://doi.org/10.1007/s11270-025-08281-8

Qiang, S., Shi, X., Kang, X., Revil, A., 2022. Optimized arrays for electrical resistivity tomography survey using Bayesian experimental design. Geophysics 87, E189–E203. https://doi.org/10.1190/geo2021-0408.1

Radosavljevic, J., Slowinski, S., Rezanezhad, F., Shafii, M., Gharabaghi, B., Van Cappellen, P., 2024. Road Salt-induced salinization impacts water geochemistry and mixing regime of a Canadian urban lake. Appl. Geochem. 162, 105928. https://doi.org/10.1016/j.apgeochem.2024.105928. https://linkinghub.elsevier.com/retrieve/pii/S0883292724000337.

Rücker, C., Günther, T., Wagner, F.M., 2017. pyGIMLi: an open-source library for modelling and inversion in geophysics. Comput. Geosci. 109, 106–123. https://doi.org/10.1016/j.cageo.2017.07.011. https://linkinghub.elsevier.com/retrieve/pii/S0098300417300584.

Shannon, T.P., Ahler, S.J., Mathers, A., Ziter, C.D., Dugan, H.A., 2020. Road Salt impact on soil electrical conductivity across an urban landscape. J. Urban Ecol. 6, juaa006. https://doi.org/10.1093/jue/juaa006. https://academic.oup.com/jue/article/doi/10.1093/jue/juaa006/5741239.

Shuster, W., Schifman, L., Kelleher, C., Golden, H.E., Bhaskar, A.S., Parolari, A.J., Stewart, R.D., Herrmann, D.L., 2021. *k* in an urban world: new contexts for hydraulic conductivity. JAWRA J. Am. Water Resour. Assoc. 57, 493–504. https://doi.org/10.1111/1752-1688.12918

Singh, G., Kaur, G., Williard, K., Schoonover, J., Kang, J., 2018. Monitoring of water and solute transport in the vadose zone: a review. Vadose Zone J. 17, 1–23. https://doi.org/10.2136/vzj2016.07.0058

Slater, L., Binley, A., 2021. Advancing hydrological process understanding from long-term resistivity monitoring systems. WIREs Water 8, e1513. https://doi.org/10.1002/wat2.1513

Slater, L., Binley, A., Daily, W., Johnson, R., 2000. Cross-hole electrical imaging of a controlled saline tracer injection. J. Appl. Geophys. 44, 85–102. https://doi.org/10.1016/S0926-9851(00)00002-1. https://linkinghub.elsevier.com/retrieve/pii/S0926985100000021.

Song, Y., Jiang, G., Chen, Y., Zhao, P., Tian, Y., 2017. Effects of chloride ions on corrosion of ductile iron and carbon steel in soil environments. Sci. Rep. 7, 6865. https://doi.org/10.1038/s41598-017-07245-1. https://www.nature.com/articles/s41598-017-07245-1.

Spraakman, S., Drake, J.A.P., 2021. Hydrologic and soil properties of mature bioretention cells in Ontario, Canada. Water Sci. Technol. 84, 3541–3560. https://doi.org/10.2166/wst.2021.464. https://iwaponline.com/wst/article/84/12/3541/84879/Hydrologic-and-soil-properties-of-mature.

Sterling, S.M., Ducharne, A., Polcher, J., 2013. The impact of global land-cover change on the terrestrial water cycle. Nat. Clim. Change 3, 385–390. https://doi.org/10.1038/nclimate1690. https://www.nature.com/articles/nclimate1690.

Sylvain, K., Pabst, T., Dimech, A., 2019. Waste Rock Valorization in Monolayer Covers with Elevated Water Table. Environmental Engineering.

Szklarek, S., Górecka, A., Wojtal-Frankiewicz, A., 2022. The effects of road Salt on freshwater ecosystems and solutions for mitigating chloride pollution - a review. Sci. Total Environ. 805, 150289. https://doi.org/10.1016/j.scitotenv.2021.150289. https://linkinghub.elsevier.com/retrieve/pii/S0048969721053663.

Teufel, B., Sushama, L., 2021. 2 °C vs. high warming: transitions to flood-generating mechanisms across Canada. Water 13, 1494. https://doi.org/10.3390/w13111494. https://www.mdpi.com/2073-4441/13/11/1494.

Thomle, J., Peta, K., Zhong, L., Robinson, J., Johnson, T., 2023. Design and implementation of resistive grout for cross-borehole electrical imaging. J. Appl. Geophys. 105118. https://doi.org/10.1016/j.jappgeo.2023.105118. https://linkinghub.elsevier.com/retrieve/pii/S0926985123001969.

Torres, M., Fontecha, J., Walteros, J., Zhu, Z., Ahmed, Z., Rodríguez, J., Rabideau, A., 2021. City-scale optimal location planning of green infrastructure using piece-wise linear interpolation and exact optimization methods. J. Hydrol. 601, 126540. https://doi.org/10.1016/j.jhydrol.2021.126540. https://linkinghub.elsevier.com/retrieve/pii/S0022169421005874.

Tso, C.H.M., Kuras, O., Wilkinson, P.B., Uhlemann, S., Chambers, J.E., Meldrum, P.I., Graham, J., Sherlock, E.F., Binley, A., 2017. Improved characterisation and modelling of measurement errors in electrical resistivity tomography (ERT) surveys. J. Appl. Geophys. 146, 103–119. https://doi.org/10.1016/j.jappgeo.2017.09.009. https://linkinghub.elsevier.com/retrieve/pii/S0926985116306838.

Tu, M.C., Traver, R., 2019. Water table fluctuation from green infrastructure sidewalk planters in Philadelphia. J. Irrig. Drain. Eng. 145, 05018008. https://doi.org/10.1061/(ASCE)IR.1943-4774.0001369. https://ascelibrary.org/doi/10.1061/%28ASCE%29IR.1943-4774.0001369.

Uhlemann, S., Sorensen, J.P.R., House, A.R., Wilkinson, P.B., Roberts, C., Gooddy, D.C., Binley, A.M., Chambers, J.E., 2016. Integrated time-lapse geoelectrical imaging of wetland hydrological processes. Water Resour. Res. 52, 1607–1625. https://doi.org/10.1002/2015WR017932

Uhlemann, S., Wilkinson, P.B., Maurer, H., Wagner, F.M., Johnson, T.C., Chambers, J.E., 2018. Optimized survey design for electrical resistivity tomography: combined optimization of measurement configuration and electrode placement. Geophys. J. Int. 214, 108–121. https://doi.org/10.1093/gji/ggy128. https://academic.oup.com/gji/article/214/1/108/4956525.

Vereecken, H., Huisman, J.A., Bogena, H., Vanderborght, J., Vrugt, J.A., Hopmans, J.W., 2008. On the value of soil moisture measurements in vadose zone hydrology: a review. Water Resour. Res. 44, 2008WR006829. https://doi.org/10.1029/2008WR006829

Wagner, F.M., Uhlemann, S., 2021. An overview of multimethod imaging approaches in environmental geophysics. In: Advances in Geophysics, vol. 62. Elsevier, pp. 1–72. https://doi.org/10.1016/bs.agph.2021.06.001. https://linkinghub.elsevier.com/retrieve/pii/S0065268721000017.

Weatherson, W.O.W., Oswald, C.J., Roy, J.W., 2024. High-frequency data provides insight into chloride transport pathways and exceedances of chronic chloride guidelines for the protection of aquatic life in streams impacted by deicers. ACS EST Water 4, 2445–2457. https://doi.org/10.1021/acsestwater.3c00780

Wilkinson, P.B., Uhlemann, S., Meldrum, P.I., Chambers, J.E., Carrière, S., Oxby, L.S., Loke, M., 2015. Adaptive time-lapse optimized survey design for electrical resistivity tomography monitoring. Geophys. J. Int. 203, 755–766. https://doi.org/10.1093/gji/ggv329

Xia, T., Li, M., Slater, L., Hu, X., Binley, A., Ma, X., Mao, D., 2026a. The evolving roles of electrical geophysical methods for in situ remediation assessment: progress and perspectives. Water Resour. Res. 62, e2025WR043172. https://doi.org/10.1029/2025WR043172

Xia, T., Zhang, J., Zhao, R., Li, M., Li, S., Guo, L., Mao, D., 2026b. Monitoring contaminant removal during in situ chemical oxidation using cross-borehole resistivity tomography and hydrogeology. J. Hydrol. 664, 134442. https://doi.org/10.1016/j.jhydrol.2025.134442. https://linkinghub.elsevier.com/retrieve/pii/S0022169425017822.

Xu, S., Sirieix, C., Riss, J., Malaurent, P., 2017. A clustering approach applied to time-lapse ERT interpretation — case study of lascaux cave. J. Appl. Geophys. 144, 115–124. https://doi.org/10.1016/j.jappgeo.2017.07.006. https://linkinghub.elsevier.com/retrieve/pii/S0926985117306481.